Mining-induced land subsidence detection by persistent scatterer InSAR and Sentinel-1: Application to Phugiao quarries, Vietnam

Bui Xuan Nam[1*], Tran Van Anh[2], Luyen K. Bui[3], Nguyen Quoc Long[4], Le Thi Thu Ha[4], Ropesh Goyal[5]

[1] Department of Surface Mining, Hanoi University of Mining and Geology, Hanoi, Vietnam
[2] Department of Photogrammetry and Remote Sensing, Hanoi University of Mining and Geology, Hanoi, Vietnam
[3] Department of Geodesy, Hanoi University of Mining and Geology, Hanoi, Vietnam
[4] Department of Mine Surveying, Hanoi University of Mining and Geology, Hanoi, Vietnam.
[5] Indian Institute of Technology Kanpur, Kanpur-208016, Uttar Pradesh, India

* *Corresponding author: Bui Xuan Nam (buixuannam@humg.edu.vn*

Abstract. Mining activities can cause mining hazards, among them land subsidence occurring in mine areas and their vicinities. Mining-induced surface subsidence is often quantified by traditional geodetic surveying with an advantage of high accuracy, but it is usually applied in small areas. With the development of radar technology, there have been many studies applying radar interferometry technique to determine surface subsidence over wide areas at a few millimeters accuracy. In this paper, 24 Sentinel-1 SAR images are used with the persistent scatterer InSAR method to determine land subsidence of the Phugiao quarries and surrounding areas. The results are compared with average annual subsidence of 13 surveying points at the Phugiao1 mine and 16 surveying points at the Phugiao2 mine measured by global navigation satellite system (GNSS) technology from January 2018 to March 2020. The correlation coefficients of annually average land subsidence of the two methods are 0.93 and 0.82 at the two areas (Phugiao1 and Phugiao2), respectively, indicating the feasibility of applying InSAR Sentinel-1 data with the persistent scatterer InSAR method to determine surface deformation in quarries in Vietnam..

Keywords: InSAR, persistent scatterer, deformation, Sentinel-1, quarry, mine, Vietnam.

1 Introduction

Land subsidence due to exploration of natural resources such as groundwater or minerals is common in many areas of the world, e.g., in Texas [1], California (United States) [2], Bangkok (Thailand) [3], and Jakarta (Indonesia) [4]. This so-called mining hazard causes adverse impacts, which in turn result in damage to constructions [e.g., 5, 6]. Mining-induced surface subsidence is often quantified by traditional geodetic surveying using total stations, global navigation satellite system (GNSS) receivers or

terrestrial laser scanners with an advantage of high accuracy [e.g., 7, 8, 9]. However, this method is only suitable for small and accessible areas. With the development of radio detecting and ranging (radar) technology, the interferometric synthetic aperture radar (InSAR) technique can be applied effectively to determine surface subsidence over broad areas at a few millimeters accuracy [10].

Differential InSAR (DInSAR) is an InSAR technique, which was first applied to Seasat satellite imagery to study small elevation changes over an area of 50 km^2 in the Imperial Valley, California, USA [11]. This method uses at least two SAR images acquired at different times of the same location on the Earth's surface to detect the displacement by measuring the phase difference between acquisitions. However, this method has limitations because it is unable to reduce some error and noise sources, e.g., atmospheric artefacts, orbital errors [e.g., 12]. Multi-temporal InSAR (MT-InSAR) methods were therefore proposed to reduce these error and noise sources [e.g., 13]. These methods work by analyzing a network of multiple acquisitions to derive the deformation time series and thus deformation rate [e.g., 14]. Small baseline subset (SBAS) [e.g., 15, 16-21] and permanent or persistent scatter (PS) InSAR [e.g., 22, 23, 24] are among the most commonly used MT-InSAR methods. SBAS makes use of a network of multiple master images linking multiple interferograms limited in their temporal and/or perpendicular baselines, and thus increases its redundancy, particularly in case of low signal to noise ratio [25]. Persistent scatterer InSAR adopts a network of a single master image with no multilooking applied [e.g., 22, 23]; hence, it is able to detect deformation of single scatterers, and thus small objects. As a result, it is particularly appropriate for areas with highly coherent natural or man-made objects, e.g., rocks, buildings, roads [10].

The basic principle behind the PSI method is the use of a series of SAR images in the same area to extract PSs to determine land deformation. Persistent scatterer InSAR has been widely used showing good results of land deformation detection at an accuracy of up to a few millimeters [10]. For example, López-Quiroz, Doin, Tupin, Briole and Nicolas [18] applied 38 Envisat Advanced Synthetic Aperture Radar (Envisat ASAR) images to determine subsidence in Mexico City. Liu, Luo, Chen, Huang and Ding [26] used 26 European remote-sensing satellite 1/2 (ERS1/2) images to determine subsidence in Shanghai, China. In Indonesia, radar technology was applied for the first time in land subsidence determination over Jakarta in 2001 [27]. In this study, 17 Japan Earth Resources Satellite-1 (JERS-1) SAR images acquired from February 1993 to September 1998 were used to form 41 interferometric pairs relying on the PSI method with spatial baselines of 1000 m or less. The research shows that, during the period of 1993-1995, Jakarta was subsided ten centimeters, whilst from 1995 to 1998 subsidence was six centimeters.

In addition to using radar imagery to identify urban subsidence, InSAR has also been applied in mining-induced land subsidence [e.g., 28, 29-32]. Baek, Kim, Park, Jung, Kim and Kim [33] applied JERS-1 images with the small baseline subsets (SBAS) method to determine surface subsidence of Gangwon-do coal mines, Korea with the standard deviation of subsidence estimated being 7.8 mm. He, Liu and Yue [34] determined land subsidence of the Hebei mine, China by DInSAR. Diao, Wu, Hu, Li and Zhou [35] used a series of SAR images to identify subsidence of Hainan coal mines, China. The above-mentioned studies applied different MT-InSAR methods. For

instance, Diao, Wu, Hu, Li and Zhou [35] utilized the advantage DInSAR method with probability integration to detect the settlement on a large scale, while Ma, Cheng, Yang, Zhang, Guo and Zou [36] applied the SBAS method to determine land subsidence of Bu'ertai Mine, Shendong coalfield, China.

In Vietnam, the application of InSAR to determine land subsidence are mainly limited to urban areas, e.g., Hanoi and Ho Chi Minh cities. For example, Tran, Tran, Nguyen, Ho, Tran, Nguyen and Luong [37] used 27 Italian space agency (ASI)'s constellation of small satellites for Mediterranean basin observation (COSMO-SkyMed) images to determine subsidence of Hanoi urban areas due to groundwater extraction. Le and Nguyen [38] determined subsidence in Ho Chi Minh City using Advanced Land Observing Satellite Phased Array type L-band Synthetic Aperture Radar sensor (ALOS PALSAR) images by persistent scatterer InSAR. However, to the best of the authors' knowledge, InSAR has not been applied to determine mining-induced land surface deformation in Vietnam to date. This study therefore focuses on ground subsidence detection in Phugiao quarries, Vietnam and surrounding areas by the PSI method using Sentinel-1 data from 2018 to 2020. Sentinel-1 are selected in this study thanks to its free accessibility with regularly repeated acquisition at a 12-day interval, which makes it a great data source for monitoring surface deformation in mining areas. GNSS measurements observed at some locations surrounding the study area at the same time of InSAR acquisitions are adopted for validation.

The remainder of this study is structured as follow: Section **Error! Reference source not found.** introduces the study area. In Section 0, research method is described. Data used and processing steps employed in this study are described in Section 0. Section 0 discusses the experimental results and Section 0 concludes the study.

2. Study area and data

2.1 Study area

Phugiao quarries are located in Binh Duong province, which is of many different types of land and suitable for industrial plantations, civil construction and industrial development [Report investigating and evaluating the exploitation, processing situation and proposing the management remedies to protect mineral resources in Phugiao district, in Vietnames]. Until now, there have been 35 companies for mining with more than 1400 hectares in Binh Duong province [39]. In addition, Binh Duong has many special mineral resources, e.g., magmatic or weathered rocks, sediments. These mineral resources provide the province's traditional industries such as ceramics, construction materials and mining.

The study area of Phugiao quarries is located in Phugiao district, Binh Duong province with the coordinates ranging from 11°11' to 11° 29' north latitude, and 106° 38' to 106° 57' east longitude, bounded by the pink box in Fig. 1. There are 17 quarries, which are being exploited at different depths in which the deepest ones are the Chang Tan III and Phugiao IV mines, both currently at approximately -90 m. According to the provincial mineral exploitation plan, the quarries will be exploied down to −150 m.

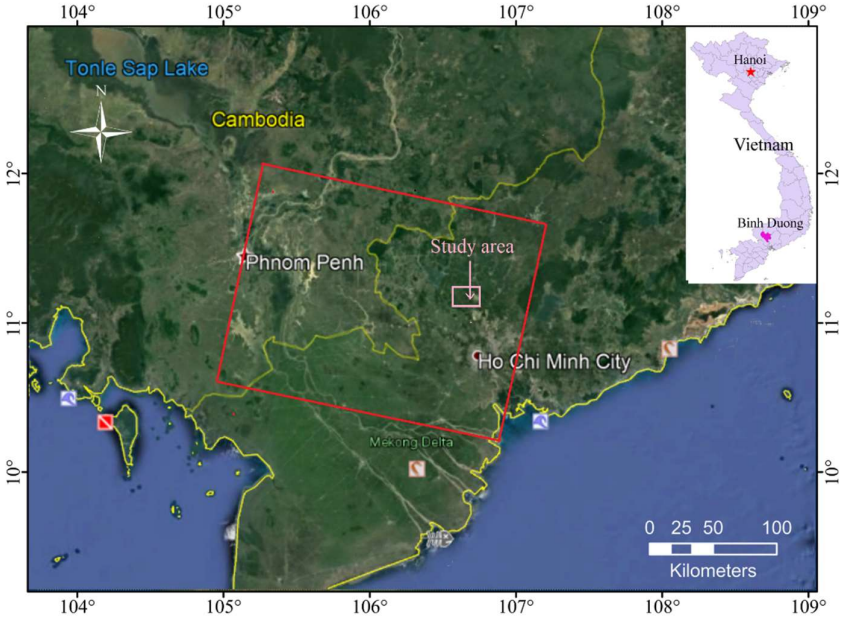

Fig. 1. The study area referred by the pink box. The red box indicate Sentinel-1 extension with three sub-swaths.

2.2 Data used

The C-band Sentinel-1 data (~5.6 cm wavelength) are utilized in this study owing to its free accessibility. Sentinel-1 satellites operate with four working modes, which are Stripmap (SM), Interferometric Wide swath (IW), Extra-Wide swath (EW), and Wave mode (WV) with different spatial resolutions. Sentinel-1 consists of two platforms currently operating in the orbit, including Sentinel-1A (launched in April 2014) and Sentinel-1B (launched in April 2016). For land surface subsidence studies applying the PSI method, images at the single look complex (SLC) format are normally adopted. In this study, SLC images at the IW mode are used. The data were downloaded from the Alaska Satellite Facilities (ASF) website of NASA [41].

In total, 24 Sentinel-1B dual polarization (VV+VH) images captured in the study area in the descending orbit, at the path number 18 and the row number 554 have been downloaded. The images were selected according to the criteria of a good weather day, no rain, and combined with the master image creates a short spatial base lines. Then the data are processed to separate the VV polarization. Details on the Sentinel-1B data used in this study, including acquired dates and perpendicular baselines with respect to the master image are shown in Table 1, with their frame extension shown in Fig. 1 by the red box.

Table 1. Sentinel-1B data used in this study. Perpendicular baseline indicates those with respect to the master image chosen as 14-Dec-2018.

Image order	Acquired data (D/M/Y)	Perpendicular baseline (m)	Image order	Acquired data (D/M/Y)	Perpendicular baseline (m)
1	12-Jan-2018	64	13	13-Apr-2019	49
2	05-Feb-2018	52	14	19-May-2019	96
3	25-Mar-2018	-45	15	12-Jun-2019	7
4	30-Apr-2018	76	16	18-Jul-2019	34
5	05-Jun-2018	-64	17	23-Aug-2019	65
6	04-Aug-2018	38	18	28-Sep-2019	138
7	09-Sep-2018	42	19	22-Oct-2019	44
8	03-Oct-2018	90	20	15-Nov-2019	118
9	08-Nov-2018	26	21	21-Dec-2019	40
10	14-Dec-2018	master	22	26-Jan-2020	107
11	07-Jan-2019	102	23	19-Feb-2020	73
12	08-Mar-2019	106	24	26-Mar-2020	82

3. Research Method

Persistent scatterer InSAR uses multi-temporal SAR images, which relies on the DInSAR method. Assuming there is a point P located on the ground and there are two images acquired at different times (see Fig. 2), the phase difference between the two images can be extracted to determine the land deformation as:

$$\Delta\varphi_{int} = \varphi_S - \varphi_M = \frac{SP' - MP}{\frac{\lambda}{4\pi}} + \varphi_{scatt\_S} - \varphi_{scatt\_M} \quad (1)$$

where $\Delta\varphi_{int}$ is the phase difference (i.e., the interferometric phase) between the phase of the master image (φ_M) and that of the slave image (φ_S), M and S are the satellite positions of the master and the slave images, respectively (see Fig. 2), MP and SP' are the distances from the sensor to the monitoring position at the two acquisitions, respectively, λ is the radar wavelength, φ_{scatt_M} and φ_{scatt_S} are the phase change generated during the interaction between the radar wave and the target.

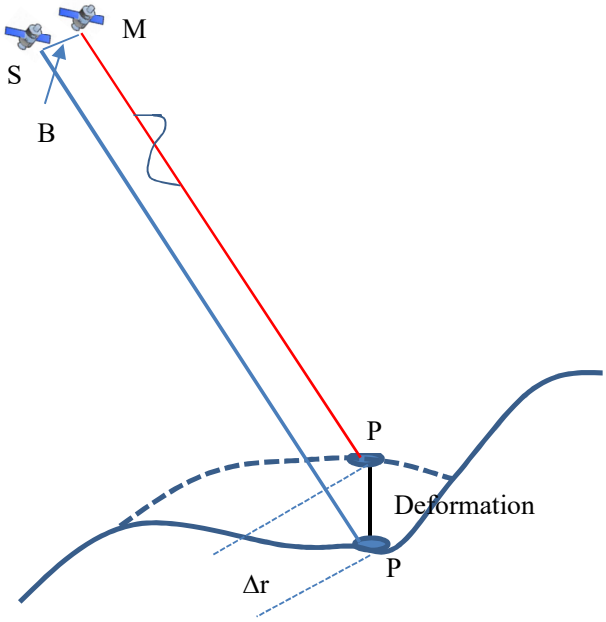

Fig. 2. DInSAR deformation measurement

The interferometric phase shown in Equation (1) includes contributions associated with topography component, surface deformation, and various error and noise sources. Therefore, to determine the land deformation, it is necessary to remove the topography component from the interferometric phase, which leads to the DInSAR method [40]:

$$\begin{aligned}\Delta\varphi_{D_{Int}} &= \Delta\varphi_{Int} - \varphi_{Topo\_simu} \\ &= \varphi_{Displ} + \varphi_{Topo\_res} + \varphi_{Atm\_S} - \varphi_{Atm\_M} + \varphi_{Orb\_S} \\ &\quad - \varphi_{Orb\_M} + \varphi_{noise} + 2.k.\pi\end{aligned} \qquad (2)$$

where $\Delta\varphi_{D_{Int}}$ is the DInSAR signal, φ_{Topo_simu} is the topographic component, φ_{Displ} corresponds to surface deformation, φ_{Topo_res} is the residual topographic error (RTE) component caused by error in digital elevation model (DEM) used, φ_{Atm_M} and φ_{Atm_S} are the atmospheric delay while the radar signal propagates through the atmosphere at the master and slave acquisitions, respectively, φ_{Orb_M} and φ_{Orb_S} are the phase components due to the orbital errors of the two images, φ_{noise} is the phase noise, k is an integer termed as phase ambiguity corresponding to the number of full wavelengths. The DInSAR technique aims at deriving surface deformation from DInSAR signal, which leads to the separation of surface deformation from other phase components in

Equation (2). An essential condition for doing so is to analyze pixels with small phase noise, which often involve objects that have strong and constant scattering characteristics over time (thus called permanent or persistent scatterers−PSs) or objects having constant scattering characteristics over time but come from small scattering objects (thus called distributed scatterers−DSs). The biggest limitation of the DInSAR method is the decrease in correlation as the time separation between master and slave acquisitions, i.e., the temporal baseline increases and the noise resulted from atmospheric delay.

The PSI method represents an improved DInSAR method, which uses multiple SAR images acquired in the same area to generate an interferogram network with a single master image. This method provides a suitable data analysis and processing procedures to separate the phase component corresponding to surface displacement from other phase components shown in Equation (2) as well as eliminate the influence of atmospheric phase screen (APS). A detail of DInSAR processing steps used in this study will be described in Section **Error! Reference source not found.**.

4. Images processing

Data processing is implemented by the Sentinel Application Platform (SNAP) [42] and the Stanford Method for Persistent Scatterer (StaMPS) [10] software. SNAP is a common architecture for all Sentinel toolboxes, which is developed jointly by Brockmann Consult, SkyWatch and C-S [42]. StaMPS is a software built to process a series of SAR scenes applying the PS and SBAS methods. StaMPS was developed originally at Stanford University, U.S but subsequent versions were developed by research groups at the University of Leeds, UK, University Iceland and Delft University of Technology, Netherlands [43].

Data processing applying the PSI method by the two software consists of two independent tasks: (i) processing DInSAR for the master image and preparing slave images by SNAP, and (ii) persistent scatterer InSAR analysis by StaMPS. Fig. 3 depicts a persistent scatterer InSAR data processing flow chart using SNAP and StaMPS. Details on these steps will be described in the following sections.

a. Preparation of the master image

In the first step, the master image is selected from the dataset in such a way to reduce the overall temporal and perpendicular baselines (see Table 1). The image acquired on 14-Dec-2018 is selected as the master image with the interferogram network being shown in Fig. 4. This master image is imported into SNAP. The subswath 1 (IW1) that fully covers the study area is then selected (see Fig. 1 for the subswath that is selected in this study). and accurating for the orbit of the Sentinel-1 image by Graph Builder function in SNAP which ability to run the command automatically. These steps are important as it will help in optimizing the subsequent processing in terms of the time consumption and resources [44].

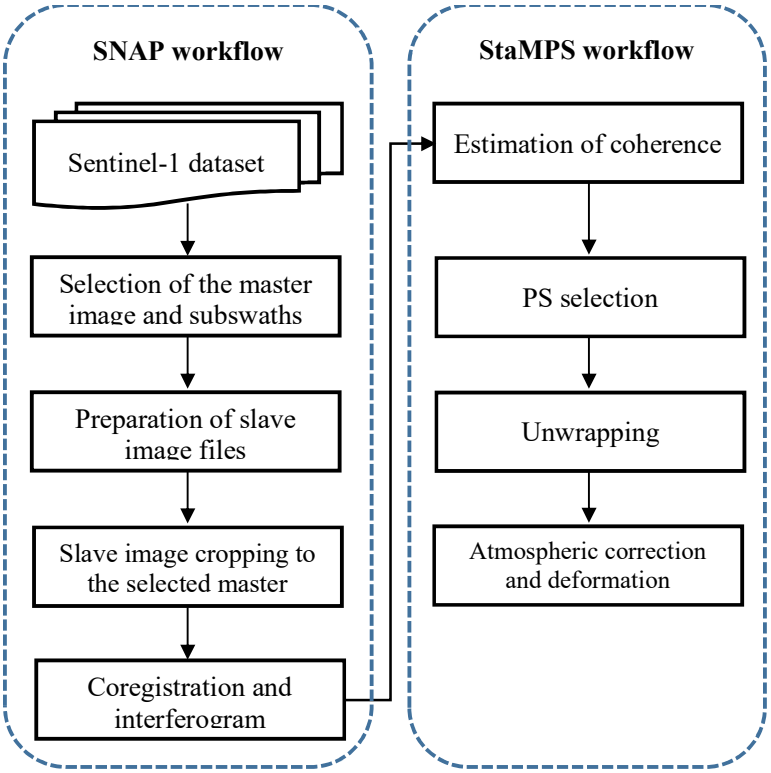

Fig. 3. Persistent scatterer InSAR data processing flow chart using SNAP and StaMPS.

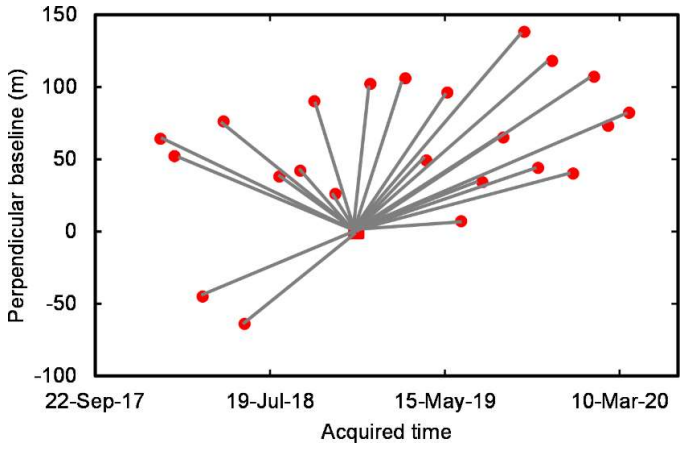

Fig. 4. Interferogram network with the image acquired on 14-Dec-2018 chosen as the master image indicated by the red square.

b. Preparation of slave images

In this step, the remaining images other than the selected master image are sorted by their acquired dates, and also checks and reduces the name of the original image file. From this step, to enable processing in batch mode, a Graph Processing Tool (GPT) is used. The Python 2.7 code used to run the processing is available on Github [45].

c. Image cropping and orbit update

Slave images are separated based on the part and the polarization, which has been determined from the master image preparation step. Bursts between master and slaves will automatically be extracted relying on the defined area of interest (AOI) region. The orbital information of slave images are subsequently updated by automatically downloading precise orbital vectors at the ESA website [46].

d. Co-registration and interferogram formation

This step conducts co-registration between the master image and each of the slave images in sequence, which requires a lot of calculations. The interferograms corresponding to each pair of master and slave images are then generated prior to removing the flat earth phase, i.e., the phase associated with the ellipsoid. Debursting for both the SLC images and the differential interferograms is applied to remove horizontal stripes. The topographical phase is then simulated using the 3-second Shuttle Radar Topography Mission (SRTM) Digital Terrain Model (DTM), which is downloaded automatically by SNAP. This topographical component is then removed from the interferograms. In this step, the research area that have selected before is subseted.

Finally, folders will be created to save resulted interferograms. They consist of folders used to store single images of SLC views for all SAR scenes, folders in which interferograms are saved, and a folder storing the coordinates of the master image and the cropped DEM of the study area.

e. Estimation of coherence

Before importing data into STaMPS, data processed from SNAP will be prepared. An important factor to include is the value for selecting the Candidate PS pixels from the interferograms [43]. The criteria for the selection of the Candidate PS pixels in time series is called amplitude dispersion (D_A) (Equation 3) [22]. In our region, the DA value selection was 0.4.

$$D_A = \frac{\sigma_A}{m_A} \tag{3}$$

where σ_A is the standard deviation of backscatter intensity and m_A is the mean of the backscatter intensity.

After converting the data into the format of MATLAB for PS processing, the next step is to perform the coherence calculation which means calculating the spatial correlation for each candidate PS pixel.

Coherence is estimated by cross correlation operation between the complex images and is performed over a local window surrounding each pixel. The complex coherence (complex correlation coefficient) between two complex SAR images u_1 and u_2 is defined as [47], [48].

$$\gamma = \frac{\sum u_1 \bar{u}_2}{\sqrt{\sum |u_1|^2 \sum |u_2|^2}} \tag{4}$$

where u_1 and u_2 are corresponding complex values from two images.

f. PSs Selection

The selection of PSs based on the probability, by comparing the results for data with random phase. Then pixels selected are weeded and dropping those that are due to signal contribution from neighbouring ground resolution elements and those deemed too noisy [43]

g. Phase unwrapping

The interferograms processed previously by SNAP are wrapped, indicating that their values vary from $-\pi$ to π; so, they need to be unwrapped by the so-called phase unwrapping, which is the most difficult step. In StaMPS, phase unwrapping can be implemented either by the 2D or 3D Minimum Cost flow (MCF) method [43]. The 3D MCF method is chosen in this study because it has been proven to be highly accurate [43]. The unwrapped interferograms are shown in Fig. 5.

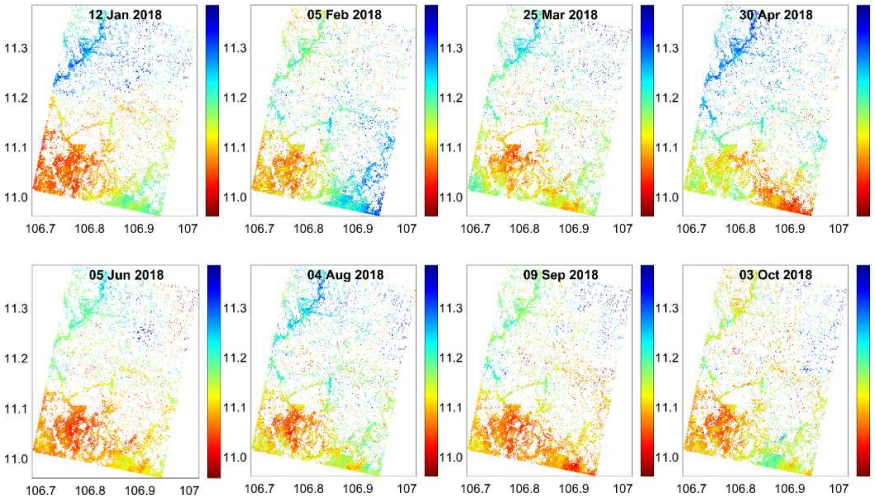

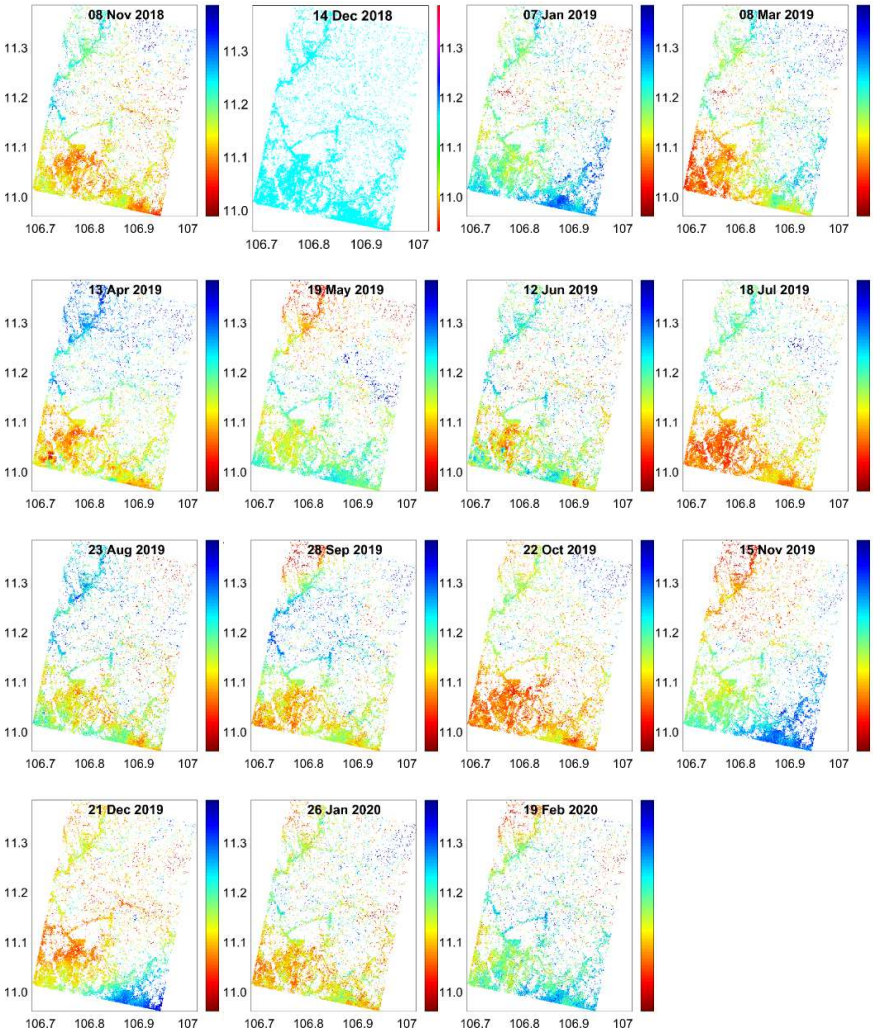

Fig. 5. Unwrapped interferograms.

h. Atmospheric correction and deformation estimation

The heterogeneity of the atmosphere (ionosphere and troposphere) and its variation over time and space cause the changes in signal's speed in the direction from the antenna and the target on the Earth's surface. This results in the phase delay termed as Atmospheric Phase Screen (APS) [43]. In this step, APS needs to be removed first, then the deformation rates are calculated from deformation time series as following: Suppose subsidence of an interest pixel is defined by $\boldsymbol{d} = [d_1, d_2, \dots, d_n], n$ being the number of the image acquisitions with their corresponding acquired times being $\boldsymbol{T} =$

$[T_1, T_2, \dots, T_n]$. The deformation rate is estimated relying on weighted least squares with the weights defined by mean square errors of the interferometric phase. The following equation is used to estimate the subsidence rate [49]:

$$\upsilon = (\boldsymbol{T}^T \boldsymbol{P} \boldsymbol{T})^{-1} \boldsymbol{T}^T \boldsymbol{P} \boldsymbol{d} \quad (5)$$

where υ is the subsidence rate, $\boldsymbol{P}$ is the vector of weights of M interferograms, which are defined by:

$$\boldsymbol{P} = diag(\sigma_1, \sigma_2, \dots, \sigma_M) \quad (6)$$

where σ_i is the mean square error of the i^{th} interferogram.

$$\mathrm{P} = \mathrm{diag}(\sigma^1, \sigma^2, \dots \sigma^{\mathrm{M}})\sigma^{\mathrm{k}}$$

5. Results and discussion

5.1 Deformation rate map

The deformation rates estimated by Equation (5) from Sentinel-1 data are displayed by the ArcGIS pro 2.5 software (Link: https://esrivn.com/arcgis-pro/) and shown in

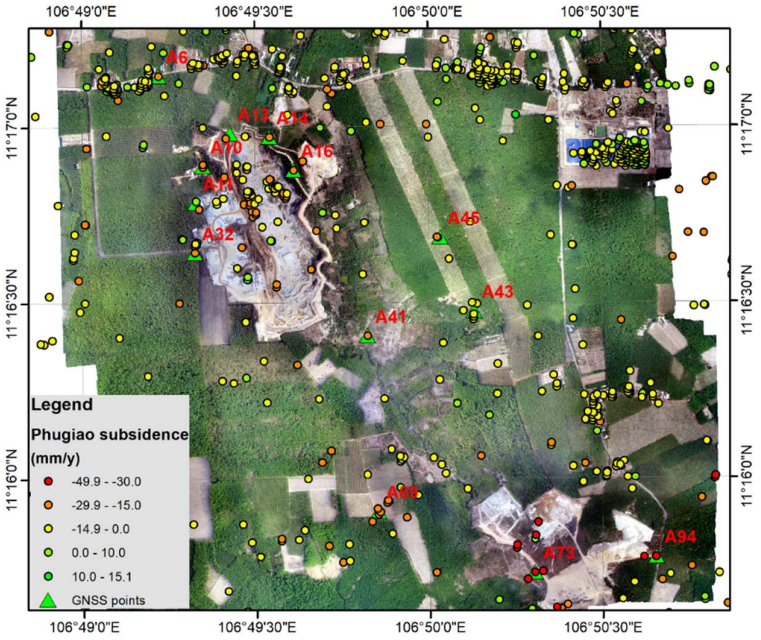

(a)

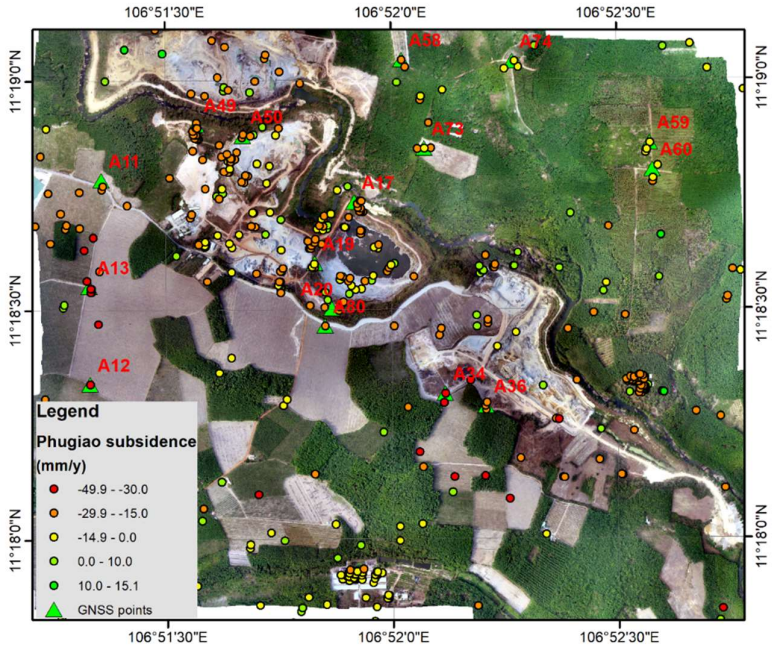

(b)

Fig. 6. Many subsidence points have been detected with the average annual rate being less than 45 mm/year. The number of points with high rate of subsidence are about 40 mm / year while the majority of subsidence is smaller than 30 mm/year. However, the sites around the mine are located on roads or houses that are our interest because these sites will directly affect people's lives.

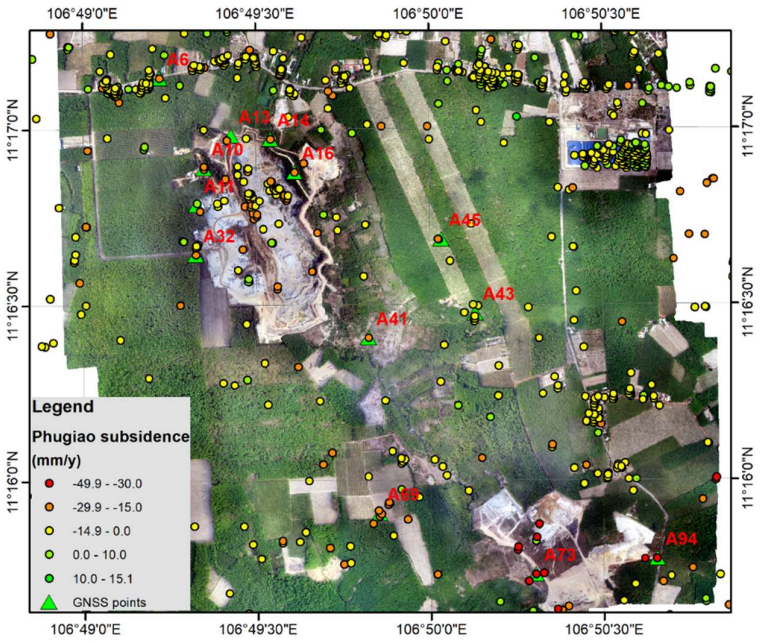
106°49'0"E
106°49'30"E
106°50'0"E
106°50'30"E
11°17'0"N
11°16'30"N
11°16'0"N
A6
A13
A14
A70
A16
A71
A45
A32
A43
A41
A69
A73
A94
Legend
Phugiao subsidence (mm/y)
-49.9 - -30.0
-29.9 - -15.0
-14.9 - 0.0
0.0 - 10.0
10.0 - 15.1
GNSS points

(a)

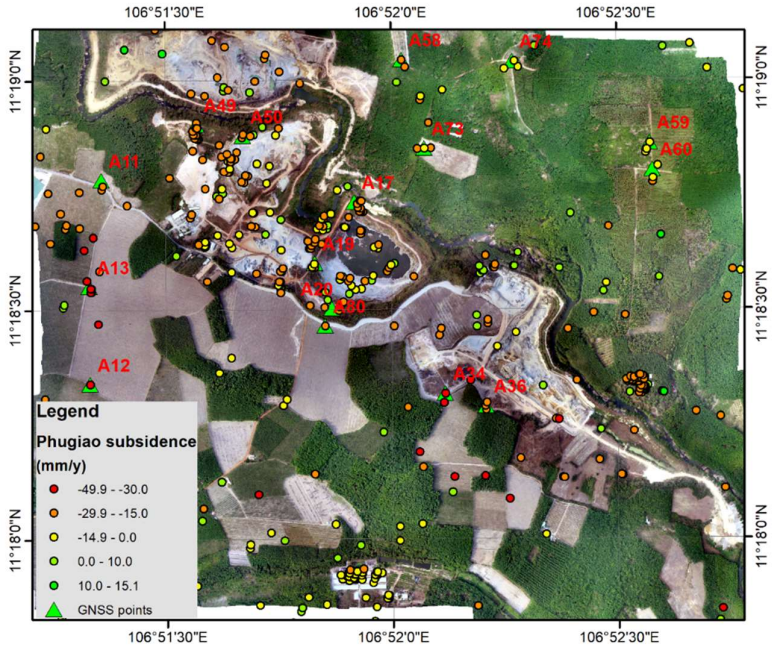

(b)

Fig. 6. Deformation rate map of the Phugiao 1 (a) and Phugiao 2 (b) quarries. The circles indicate coherent scatters and the triangles refer to GNSS stations.

5.2 Result validation

In order to validate land subsidence determined from Sentinel-1 SAR data, 20 GNSS points located throughout the entire area at locations that can represent the deformations of the Phugiao quarries are utilized. Because of its large area, the measurement method chosen was the GNSS high accuracy. The monitoring stations are connected with a 1st-grade national elevation benchmark. Before each monitoring cycle, this benchmark is measured using static mothod relying on a network connecting with two national elevation benchmarks to assess its stability in the vertical. The results indicate that it was not displaced in both measuring cycles in Feb 15-17, 2018 and March 2-4, 2020.

The static method and five CHC X91B receivers [50] are then chosen to conduct the GNSS measurement. Duration of each measument is a 180-minute. The antenna heights with respect to the station marks are read five times by stainless steel tapes. Post-processed data processing is implemented by the Trimble Business Center v3.5 (TBC 3.5) software. The root mean square error (RMSE) of the weakest point in the network are 5 mm and 4 mm in 2018 and 2020 measuring cycles, respectively.

The InSAR and GNSS subsidence results are then compared. GNSS measurement data at the monitoring points in January 2018 and December 2019 were used to calculate the average subsidence of 1 year. These are considered standard values for

comparison with the settlement results from the images of period 1 / 2018-3 / 2020. The subsidence values and the deviations between the two methods are calculated according to equation (7) and are presented in Table 2.

$$\Delta=(\Delta 1)/2-(\Delta 2)\ (mm) \quad (7)$$

where:

Δ1 – Subsidence measurement by GNSS (mm);

Δ2 - Subsidence computation from Sentinel-1 images (mm/y).

Table 2. Subsidence measurement values by GNSS and Sentinel-1 images (Phugiao1)

Number	Station name	GNSS subsidence Δ1 (mm)	InSAR subsidence Δ2 (mm/y)	Deviation Δ (mm/y)
1	A10	-15.8	-11.6	3.7
2	A11	-26.2	-12.2	-0.9
3	A13	-30.5	-19.5	4.25
4	A14	-35.2	-21.1	3.5
5	A16	-35.1	-18.8	1.25
6	A43	-14.2	-4.7	-2.4
7	A45	-15.6	-10.3	2.5
8	A73	-66.3	-35.1	1.95
9	A6	-27.2	-13	-0.6
10	A32	-49.2	-25.9	1.3
11	A69	-30.3	-19.1	3.95
12	A94	-64.7	-35.5	3.15
13	A41	-48.6	-25.2	0.9

Table 3. Subsidence measurement values by GNSS and Sentinel-1 images (Phugiao2)

Number	Station name	GNSS subsidence Δ1 (mm)	InSAR Subsidence Δ2 (mm/y)	Deviation Δ (mm/y)
1	A12	-58.2	-31.3	2.2
2	A13	-70.2	-33.6	-1.5
3	A11	-32.1	-17.4	1.35
4	A50	-37.5	-20.5	1.75
5	A49	-29.2	-16.3	1.7
6	A74	-24.3	-10.3	-1.85
7	A20	-62.3	-33.1	1.95
8	A80	-48.1	-21.9	-2.15
9	A34	-53.2	-33.7	7.1
10	A36	-50.6	-27.1	1.8
11	A60	-8.1	-7.4	3.35
12	A59	-18.5	-5.3	-3.95
13	A19	-40.5	-22.6	2.35
14	A17	-30.8	-20.1	4.7
15	A58	-58.8	-20.4	-9
16	A73	-34.6	-15.5	-1.8

5.3 Discussions

a. In mining areas

- The subsidence points from Sentinel-1 images are quite concentrated in the mine area. However, because it is an open pit mine, the surface of the mine topography is constantly changing with the exploitation process, so that the mining pits have not been surveyed in the field by GNSS.
- Although there is not any GNSS measurement data to validate subsidence at the mine pits, from the comparison results in Table 2 which is the subsidence survey sites by GNSS and the PS points located near the quarry or on roads close to the open pits. It can be seen that the subsidence values from the images are quite similar to the result from the GNSS measurement, with accuracy ± 2.6 mm at Phugiao1 and ±3.7 mm at Phugiao2. Therefore, the results of subsidence at the open pit sites are considered accurate. With the determined values of subsidence in the mine area, we can note some locations with large values of subsidence, such as at locations A, B (Phugiao1) and C, D (Phugiao2) (Fig.6) which are concentrated on the pits and the transport routes.
- For A position, the maximum value of subsidence is about -40 mm/year with red PS points, orange PS points with subsidence values less than -20 mm/year. At B position, the number of distribution subsidence points are more than the A position but the subsidence values are not as high as those in A position (see the chart in Fig.6). Subsidence values are mostly less than -30 mm/year. At C position, the average of subsidence is about -30mm / year, there are some PS points with subsidence close to -50mm/year but almost the PS points are from -10mm/year to -30mm/year. At D position, the majority of subsidence ranges from -10 mm/year to -25 mm/year. In this site there are some positive points also. The reason for the occurrence of PS points with both positive and negative values in the mining pits is partly due to the drilling and blasting operations and the work of heavy trucks are also a cause of the positive deformation.

b. In locations adjacent to open-pit mines

At the positions located on the roads or residential areas surrounding open-pit mines, we conducted assessment 13 points at Phugiao 1 and 16 points at Phugiao2 respectively which concentrated locations of PS points with the distribution near or outside within a radius of about 20 m. These points are listed in Table 2 and Table 3 above. The reason for the selection of points within this 20 m radius is due to the scattering properties of the radar image when the Radar wave reaches the surface of the object, the reflected scattering rays may not return immediately but it may be corner backscattering or

volume scattering before returning, thus the checkpoints shown on the image may be slightly shifted from its actual position.

Based on Table 2, the GNSS measurements have 2 years interval while the measurements from 24 Sentinel-1 image processing are averaged over the period from January 2018 to March 2020. So the values of subsidence measurements using GNSS will have to be divided by an average of 2 years. The correlation of these 20 points was evaluated for the purpose of a preliminary assessment of how the subsidence points measured by the PSI method achieved compared to the high precision GNSS measurement method. Below is the distribution of ground settlement values of the 13 locations shown in Table 2 and 16 locations in Table 3.

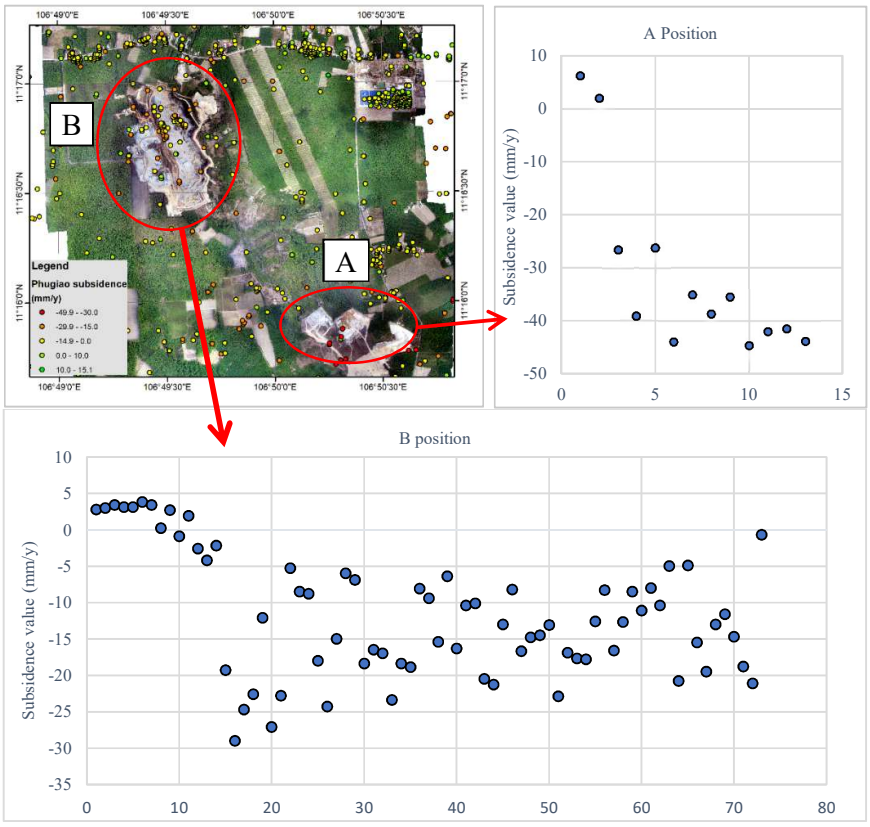

(a)

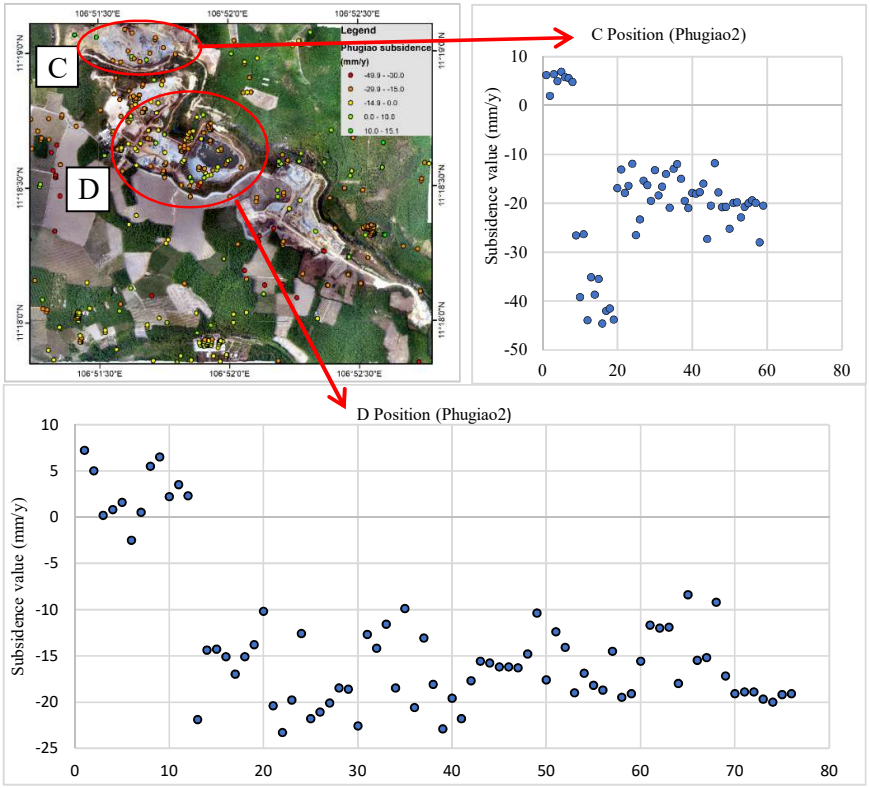

(b)

Fig. 6: Subsidence in A, B (a) and C, D (b) with the charts of subsidence values

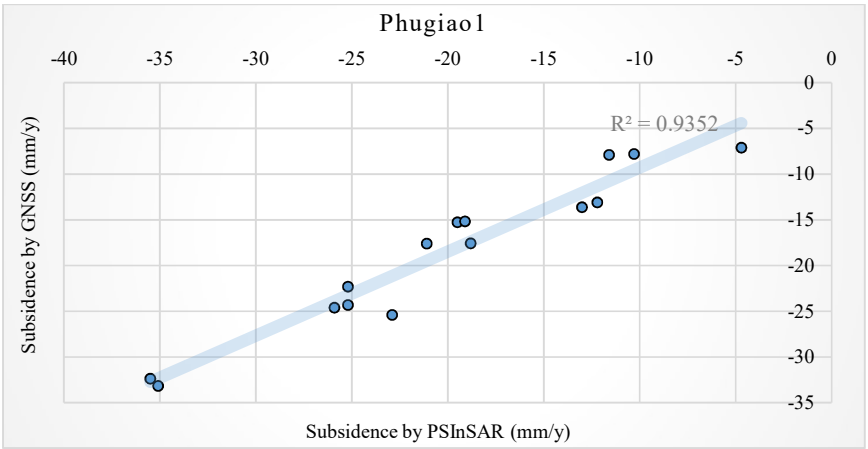

(a)

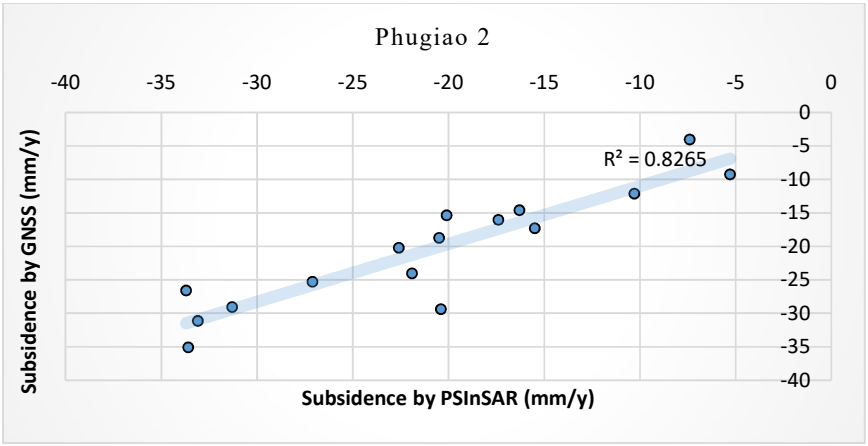

(b)

Fig. 7: The chart of the correlation of subsidence results made by Sentinel-1 radar and GNSS measurement at Phugiao1 (a) and Phugiao2 (b)

Based on the chart in Fig. 7, it is to recognize that the settlement values made from the PSI method tend to be higher than the settlement values measured from GNSS high accuracy method, however, the correlation is quite good with R2 reached 0.93 and 0.82 at two sites. This can also be explained easily because the number of survey points is not much and in addition, the GNSS and PS points from the image are not completely overlapping. Although the number of checkpoints is not much (31 points), the measured values also reflect the subsidence situation around the Phugiao open-pit mines in the period from January 2018 to March 2020.

6. Conclusions

With a data set of 24 Sentinel-1B images collected between January 2018 and March 2020, the PSI method was applied with the combination of ESA SNAP and StaMPS software. The results of determining the land subsidence of Phugiao open pit and surround area indicate the following:

The PSI method is suitable for mining areas with few trees and as many constructions as this study area. Sentinel-1 image with a resolution of 3.5m in range and 22 m in azimuth, large cover and high frequency of image acquisitions (12 days), is very appropriate for studies related to land subsidence.

This is the first time, the issue of land subsidence in mining areas in Vietnam has been investigated by using a combination of radar intermerometric method and GNSS method. With a large number of images, the rate of land subsidence was evaluated within a period of approximately 2 years and 3 months. In the quarry area there were many subsidence PS points, but these subsidence points were mostly located on the road of pits or the slope of the mining pits. The biggest land subsidence rate at mines was smaller than -45mm/year.

In the area around the quarry such as roads, edge of pits or houses near the mines have been surveyed by GNSS. Persistent scatterer InSAR subsidence points were compared to GNSS measurement points from January 2018 to December 2019. However, the number of GNSS measurement points and PS points from radar images did not completely coincide, we used 31 locations around the mine area where PS subsidence points coincided with those measured by GNSS in radius of 20 m. Correlation of these two data types reached 0.93 and 0.82 at Phugiao1 and Phugiao2 respectively, proving the ability to determine land subsidence by the Sentinel-1 image sequence.

Acknowledgments

This work is supported financially by Research Institute for Mining Electro-Mechanics of Hanoi University of Mining and Geology. The authors also thank Alaska Satellite Facilities (ASF) for providing Sentinel-1 InSAR data and colleagues from Department of Mine Surveying for providing the GNSS data.

Conflicts of interest

The authors declare no conflict of interest.

References

1. Bawden, G.W., Johnson, M.R., Kasmarek, M.C., Brandt, J.T., Middleton, C.S.: Investigation of land subsidence in the Houston-Galveston region of Texas by using the global positioning system and interferometric synthetic aperture radar, 1993-2000. US Geological Survey (2012)
2. Tizzani, P., Berardino, P., Casu, F., Euillades, P., Manzo, M., Ricciardi, G., Zeni, G., Lanari, R.: Surface deformation of Long Valley caldera and Mono Basin, California, investigated with the SBAS-InSAR approach. Remote Sensing of Environment 108, 277--289 (2007)
3. Aobpaet, A., Cuenca, M.C., Hooper, A., Trisirisatayawong, I.: InSAR time-series analysis of land subsidence in Bangkok, Thailand. International Journal of Remote Sensing 34, 2969--2982 (2013)
4. Ng, A.H.-M., Ge, L., Li, X., Abidin, H.Z., Andreas, H., Zhang, K.: Mapping land subsidence in Jakarta, Indonesia using persistent scatterer interferometry (PSI) technique with ALOS PALSAR. International Journal of Applied Earth Observation and Geoinformation 18, 232--242 (2012)
5. Yang, K., Yan, L., Huang, G., Chen, C., Wu, Z.: Monitoring building deformation with InSAR: Experiments and validation. Sensors 16, 2182 (2016)
6. Akcin, H., Kutoglu, H., Deguchi, T., Koksal, E.: Monitoring subsidence effects in the urban area of Zonguldak Hardcoal Basin of Turkey by InSAR-GIS integration. Natural Hazards and Earth System Sciences 10, 1807--1814 (2010)

7. Gao, J.-x., Chao, L., Jian, W., LI, Z.-k., MENG, X.-c.: A new method for mining deformation monitoring with GPS-RTK. Transactions of Nonferrous Metals Society of China 21, s659-s664 (2011)
8. Lian, X., Hu, H.: Terrestrial laser scanning monitoring and spatial analysis of ground disaster in Gaoyang coal mine in Shanxi, China: a technical note. Environmental Earth Sciences 76, 287 (2017)
9. Tiwari, A., Narayan, A.B., Dwivedi, R., Swadeshi, A., Pasari, S., Dikshit, O.: Geodetic investigation of landslides and land subsidence: case study of the Bhurkunda coal mines and the Sirobagarh landslide. Survey Review 52, 134-149 (2020)
10. Hooper, A., Bekaert, D.P.S., Spaans, K., Arıkan, M.: Recent advances in SAR interferometry time series analysis for measuring crustal deformation. Tectonophysics 514-517, 1-13 (2012)
11. Graham, L.C.: Synthetic interferometer radar for topographic mapping. Proceedings of the IEEE 62, 763--768 (1974)
12. Tran, A.V., Masumoto, S., Raghavan, V., Shiono, K.: Spatial distribution of subsidence in Hanoi detected by JERS-1 SAR interferometry. Japan Society of Geoinformatics 18, 3--13 (2007)
13. Hooper, A.: A multi-temporal InSAR method incorporating both persistent scatterer and small baseline approaches. Geophysical Research Letters 35, L16302 (2008)
14. Shanker, P., Casu, F., Zebker, H.A., Lanari, R.: Comparison of persistent scatterers and small baseline time-series InSAR results: A case study of the San Francisco bay area. IEEE Geoscience and Remote Sensing Letters 8, 592-596 (2011)
15. Berardino, P., Fornaro, G., Lanari, R., Sansosti, E.: A new algorithm for surface deformation monitoring based on small baseline differential SAR interferograms. IEEE Transactions on Geoscience and Remote Sensing 40, 2375-2383 (2002)
16. Cavalié, O., Doin, M.P., Lasserre, C., Briole, P.: Ground motion measurement in the Lake Mead area, Nevada, by differential synthetic aperture radar interferometry time series analysis: Probing the lithosphere rheological structure. Journal of Geophysical Research: Solid Earth 112, 1-18 (2007)
17. Hetland, E.A., Musé, P., Simons, M., Lin, Y.N., Agram, P.S., DiCaprio, C.J.: Multiscale InSAR Time Series (MInTS) analysis of surface deformation. Journal of Geophysical Research: Solid Earth 117, B02404 (2012)
18. López-Quiroz, P., Doin, M.-P., Tupin, F., Briole, P., Nicolas, J.-M.: Time series analysis of Mexico City subsidence constrained by radar interferometry. Journal of Applied Geophysics 69, 1--15 (2009)
19. Lundgren, P., Usai, S., Sansosti, E., Lanari, R., Tesauro, M., Fornaro, G., Berardino, P.: Modeling surface deformation observed with synthetic aperture radar interferometry at Campi Flegrei caldera. Journal of Geophysical Research: Solid Earth 106, 19355-19366 (2001)
20. Schmidt, D.A., Bürgmann, R.: Time-dependent land uplift and subsidence in the Santa Clara valley, California, from a large interferometric synthetic aperture radar data set. Journal of Geophysical Research: Solid Earth 108, (2003)
21. Usai, S.: A Least Squares Database Approach for SAR Interferometric Data. IEEE Transactions on Geoscience and Remote Sensing 41, 753-760 (2003)

22. Ferretti, A., Prati, C., Rocca, F.: Permanent scatterers in SAR interferometry. IEEE Transactions on geoscience and remote sensing 39, 8--20 (2001)
23. Hooper, A.: Persistent scatter radar interferometry for crustal deformation studies and modeling of volcanic deformation. ProQuest Dissertations Publishing (2006)
24. Hooper, A., Segall, P., Zebker, H.A.: Persistent scatterer interferometric synthetic aperture radar for crustal deformation analysis, with application to Volcán Alcedo, Galápagos. Journal of Geophysical Research: Solid Earth 112, (2007)
25. Bui, L.K., Featherstone, W.E., Filmer, M.S.: Disruptive influences of residual noise, network configuration and data gaps on InSAR-derived land motion rates using the SBAS technique. Remote Sensing of Environment 247, 111941 (2020)
26. Liu, G., Luo, X., Chen, Q., Huang, D., Ding, X.: Detecting land subsidence in Shanghai by PS-networking SAR interferometry. Sensors 8, 4725--4741 (2008)
27. Hirose, K., Maruyama, Y., Murdohardono, D., Effendi, A., Abidin, H.Z.: Land subsidence detection using JERS-1 SAR Interferometry. In: 22nd Asian Conference on Remote Sensing, pp. 5--9. (Year)
28. Yang, Z., Li, Z., Zhu, J., Feng, G., Wang, Q., Hu, J., Wang, C.: Deriving time-series three-dimensional displacements of mining areas from a single-geometry InSAR dataset. Journal of Geodesy 92, 529--544 (2018)
29. Gee, D., Bateson, L., Sowter, A., Grebby, S., Novellino, A., Cigna, F., Marsh, S., Banton, C., Wyatt, L.: Ground motion in areas of abandoned mining: application of the intermittent SBAS (ISBAS) to the Northumberland and Durham Coalfield, UK. Geosciences 7, 85 (2017)
30. Zheng, M., Deng, K., Du, S., Liu, J., Liu, J., Feng, J.: Joint Probability Integral Method and TCPInSAR for Monitoring Mining Time-Series Deformation. Journal of the Indian Society of Remote Sensing 47, 63--75 (2019)
31. Zhu, Y., Ding, X., Li, Z., Luo, Y.: Monitoring of Surface Subsidence of the Mining Area Based on SBAS. JCP 9, 1177--1184 (2014)
32. Ng, A.H.-M., Ge, L., Du, Z., Wang, S., Ma, C.: Satellite radar interferometry for monitoring subsidence induced by longwall mining activity using Radarsat-2, Sentinel-1 and ALOS-2 data. International journal of applied earth observation and geoinformation 61, 92--103 (2017)
33. Baek, J., Kim, S.-W., Park, H.-J., Jung, H.-S., Kim, K.-D., Kim, J.W.: Analysis of ground subsidence in coal mining area using SAR interferometry. Geosciences Journal 12, 277--284 (2008)
34. He, J., Liu, G., Yue, H.: Monitoring ground subsidence in mining area using spaceborne InSAR technology. In: 2009 Joint Urban Remote Sensing Event, pp. 1--6. IEEE, (Year)
35. Diao, X., Wu, K., Hu, D., Li, L., Zhou, D.: Combining differential SAR interferometry and the probability integral method for three-dimensional deformation monitoring of mining areas. International Journal of Remote Sensing 37, 5196--5212 (2016)
36. Ma, C., Cheng, X., Yang, Y., Zhang, X., Guo, Z., Zou, Y.: Investigation on mining subsidence based on multi-temporal InSAR and time-series analysis of the small baseline subset—Case study of working faces 22201-1/2 in Bu'ertai mine, Shendong coalfield, China. Remote Sensing 8, 951 (2016)

37. Tran, A.V., Tran, C.Q., Nguyen, A.D., Ho, D.M.T., Tran, A.T., Nguyen, H.N., Luong, L.T.T.: Application of PSInSAR method for determining of land subsidence in Hanoi city by Cosmo-Skymed imagery. Proceedings of GIS IDEAS (2016)
38. Le, T.V., Nguyen, C.T.: Assessment of capacity of using sentinel-1 images in monitoring land subsidence in Ho Chi Minh City. Science & Technology Development Journal-Science of The Earth & Environment 2, 19--25 (2019)
39. http://btv.org.vn/tin-tuc/khai-thac-khoang-san-di-doi-voi-bao-ve-moi-truong-23304.html:
40. Gabriel, A.K., Goldstein, R.M., Zebker, H.A.: Mapping small elevation changes over large areas: Differential radar interferometry. Journal of Geophysical Research: Solid Earth 94, 9183-9191 (1989)
41. https://search.asf.alaska.edu:
42. http://step.esa.int/main/toolboxes/snap/:
43. Hooper, A., Spaans, K., Bekaert, D., Cuenca, M.C., Arıkan, M., Oyen, A.: StaMPS/MTI manual. Delft Institute of Earth Observation and Space Systems Delft University of Technology, Kluyverweg 1, 2629 (2010)
44. Delgado Blasco, J.M., Foumelis, M., Stewart, C., Hooper, A.: Measuring Urban Subsidence in the Rome Metropolitan Area (Italy) with Sentinel-1 SNAP-StaMPS Persistent Scatterer Interferometry. Remote Sensing 11, 129 (2019)
45. Foumelis, M., Blasco, J.M.D., Desnos, Y.-L., Engdahl, M., Fernández, D., Veci, L., Lu, J., Wong, C.: ESA SNAP-StaMPS Integrated Processing for Sentinel-1 Persistent Scatterer Interferometry. In: IGARSS 2018-2018 IEEE International Geoscience and Remote Sensing Symposium, pp. 1364--1367. IEEE, (Year)
46. https://qc.sentinel1.eo.esa.int/:
47. Lee, J.-S., Hoppel, K.W., Mango, S.A., Miller, A.R.: Intensity and phase statistics of multilook polarimetric and interferometric SAR imagery. IEEE Transactions on Geoscience and Remote Sensing 32, 1017-1028 (1994)
48. Bamler, R., Just, D.: Phase statistics and decorrelation in SAR interferograms. In: Proceedings of IGARSS'93-IEEE International Geoscience and Remote Sensing Symposium, pp. 980-984. IEEE, (Year)
49. Jiang, Y., Liao, M., Wang, H., Zhang, L., Balz, T.: Deformation monitoring and analysis of the geological environment of Pudong international airport with persistent scatterer SAR interferometry. Remote Sensing 8, 1-18 (2016)
50. https://nguyenkimjsc.vn/may-gps-rtk-chc-x91b.html: